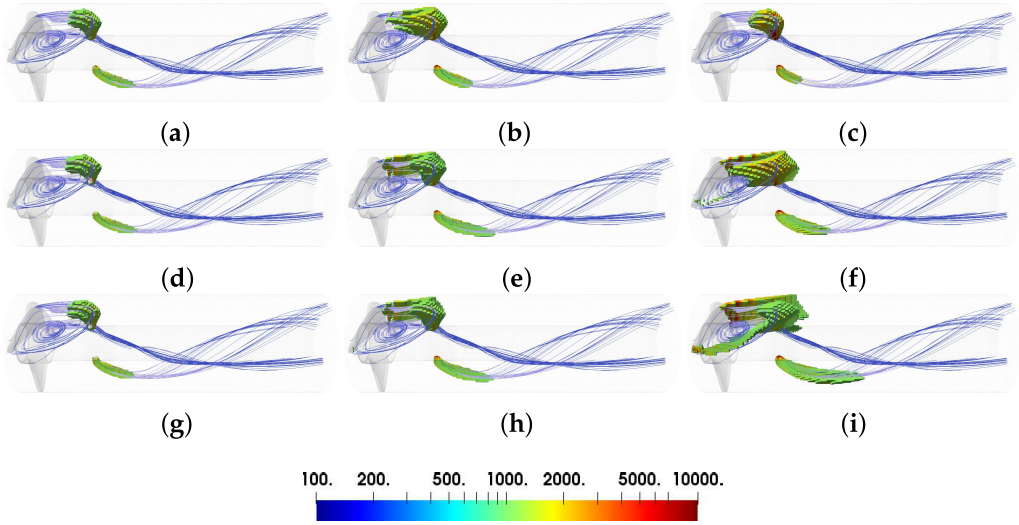

Figure 7. Supersaturation fields. The volumes represented correspond to cells whose supersaturation values are greater than 1000.

Figure 7 illustrates the supersaturation levels obtained within the system. The visualized volumes correspond to computational cells where supersaturation exceeds 1000. The colorbar scale was adjusted to enhance clarity. According to Equation (14), local supersaturation is primarily influenced by the OH^- concentration. When $\bar{\alpha}_s$ shows minimal variation with increasing Mg^{2+} concentration (Table 3, first column), the resulting supersaturation profile remains largely unaffected under constant OH^- levels (cases shown in Figure 7a,d,g). A similar trend is observed when the second column of Table 3 is examined (cases shown in Figure 7b,e,h). On the other hand, by evaluating the trend in the rows in Table 3, more pronounced changes are revealed. For example, $\bar{\alpha}_s$ decreases along the rows, indicating a worsening in mixing efficiency. Meanwhile, the OH^- concentration increases, enhancing supersaturation. These opposing effects compete with each other. As an example, in the cases shown in Figure 7a,b, the increase (doubling) in OH^- concentration dominates, leading to both higher supersaturation levels and a larger affected volume. However, when OH^- is further increased (doubled again), as shown in Figure 7b,c, the sharper decrease in $\bar{\alpha}_s$ results in a reduced supersaturation volume, demonstrating that a worsened mixing can limit precipitation despite higher reactant levels. To ensure meaningful comparisons, the simulation matrix includes case pairs with identical mixing conditions. Specifically, cases Figure 7d,h, as well as cases Figure 7e,i, share the same $\bar{\alpha}_s$ values (0.992 and 0.984, respectively). In these instances, the f term in Equation (14) remains constant, isolating the effect of increasing reactant concentrations. As expected, higher concentrations lead to an increased supersaturation and precipitation volume. Thus, unless extremely high supersaturation and extended precipitation zones are desired (as in Figure 7f,i), using lower OH^- concentrations can be advantageous. This strategy allows for comparable supersaturation profiles with reduced reagent consumption and, consequently, lower operational costs. The analysis is reinforced through the results obtained for m_0, shown in Figure 8.

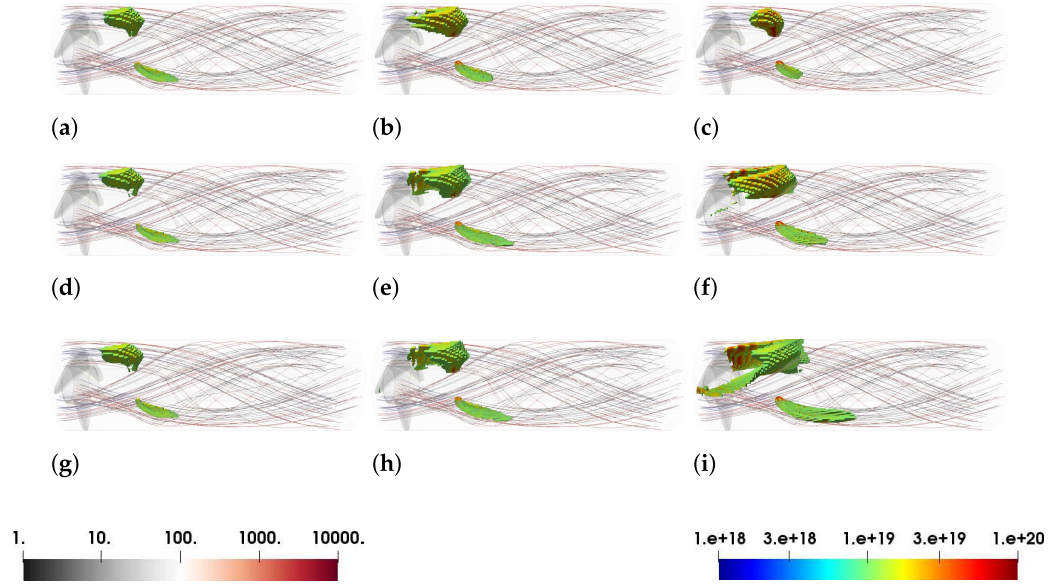

Figure 8. Representation of the ε field on the flow streamlines and m_0 fields. The volumes represented correspond to cells whose m_0 values are greater than 10^{19}.

In Figure 8, the streamlines represent the path a particle takes in the fluid, and the field reported on the streamlines is the epsilon field. It is important to note that, under constant flow and turbulence fields, the spatial distribution of supersaturation solely drives and modulates particle formation. Indeed, the zeroth moment, m_0, depends exclusively on nucleation and aggregation phenomena which, at a constant-turbulence field (ε), are governed by the local supersaturation levels. As reported in Equation (17), nucleation is a direct function of supersaturation, while aggregation is indirectly influenced through the sticking probability (Equations (19), (23) and (25)). The sticking probability depends on the crystal growth rate G, which, in turn, is a function of the local supersaturation. Therefore, the variations observed in the m_0 profiles across the different cases reflect the impact of the supersaturation field on precipitation performance when hydrodynamic conditions are fixed. For example, comparing Figure 8a,b, the increase in OH^- concentration (doubling) leads to a clear increase in m_0, both in terms of absolute values and spatial extent. This occurs despite a slight reduction in the stoichiometric mixture fraction, $\bar{\alpha}_s$. However, when the OH^- concentration is further doubled (shown in Figure 8b,c), $\bar{\alpha}_s$ decreases more significantly and a noticeable reduction in the extent of the m_0 field is observed. Therefore, the analysis of the supersaturation profiles directly informs the interpretation of the m_0 field, as similar trends and effects can be observed.

(ii) Effect of the nozzle's orientation and position

We present and discuss the results of the nozzle's orientation and position in the prototype at constant reactant concentrations and flow rates. In other words, this investigation shows the influence of turbulence on particle formation. A total of six simulations (2×3 cases) were conducted, combining different nozzle orientations (two cases) and different positions along the prototype axis (three cases). For the nozzle orientation, the mutual angular position was not changed. The nozzles were positioned at equal angular intervals of 120° around the circumference of the inner tube. The two cases shown for the orientation refer to the injection of Mg^{2+} into the zone of the circular crown with a low (L) fluid velocity and high (H) fluid velocity. It is noteworthy that the nozzle orientation was adapted to the helicoid flow field developed within the system so that the Mg^{2+} was always fed into the low-fluid-velocity or the high-fluid-velocity zone. These two cases were repeated at three axial coordinates, resulting in six simulations. For the

sake of confidentiality, the axial positions were made dimensionless and were at 0.1, 0.2, and 0.6 of the dimensionless length $\tilde{L}$. Figure 9 shows the six simulation setups reporting the velocity field when the nozzles' orientation ((L) or (H)) and position ($\tilde{L}$ = 0.1 or 0.2 or 0.6) were varied:

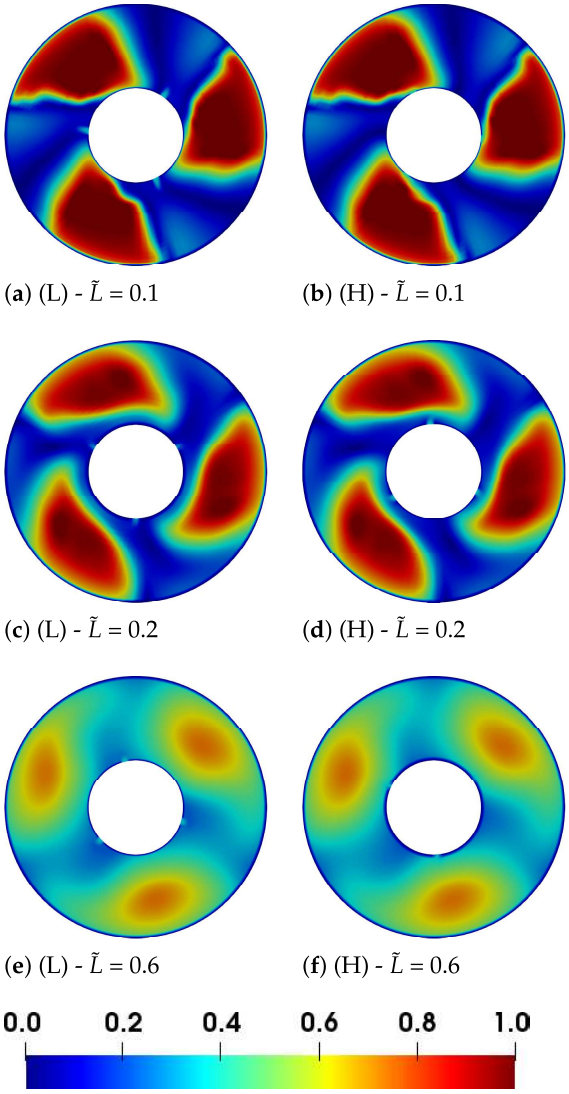

Figure 9. Nozzle configuration: velocity magnitude fields for the feed sections across the six simulated scenarios.

As is clear from Figure 9, the nozzle orientation does not affect the flow field since the Mg^{2+} flow-rate is much smaller compared to the OH^{-} one. For this reason, the ϵ field is reported for only one orientation case (H) at the three different positions along the prototype axis, as shown in Figure 10.

To ensure the same reaction volume (i.e., the same reaction length), simulations were run on a geometry comprising the investigated block plus a portion of the following block, which was equal to the investigated nozzle positions, at 0.1, 0.2, and 0.6 respectively, as reported in Figure 11.

Figures 9 and 11 show interesting results. The orientation of the nozzles has a massive impact (Figure 11a,b) when the nozzles are located at a dimensionless coordinate of 0.1. Figures 9a,b and 10a show that the flow and turbulence fields in the Mg^{2+} feed are very different for the two cases. For the (L) case (Figure 11a), Mg^{2+} reacts in a region where velocity and local turbulence are smaller. It follows that mixing is slower and aggregation

is less favored, as it is directly proportional to $\sqrt{\varepsilon}$. This is the reason why a larger prototype volume has higher m_0 values. Particles nucleate and grow more than they aggregate. On the other hand, for the (H) case (Figure 11b) the Mg^{2+} reacts in a region where velocity and local turbulence are much more intense. It follows that mixing is much faster and aggregation much more intense as it is demonstrated by the evolution m_0. At a dimensionless coordinate of 0.2, the effect becomes less intense, as shown in Figure 11c,d. Figure 9c,d show that the vortex is no longer adjacent to the inner tube and, consequently, the local turbulence found in both cases is similar (Figure 10b). The main change in the m_0 profiles depends on the vortex that the three Mg^{2+} jets encounter. Finally, the effect of the nozzle orientation at a dimensionless coordinate of 0.6 (Figure 11e,f) is practically negligible. This is due to the flow (Figure 9e,f) and turbulence (Figure 10c) fields, which become dampened (and homogenized) by the pressure drops. Therefore, regardless of the orientation, the three nozzles see similar turbulence levels, and the trend of m_0 is nearly the same. To conclude, depending on the manufacturing goal, a decision can be made [31]. If larger particles are preferred, a condition closer to the one in Figure 11a should be preferred. On the other hand, if aggregates are required, a condition in which mixing is faster and turbulence is more intense, namely, a condition closer to the one in Figure 11b, should be preferred.

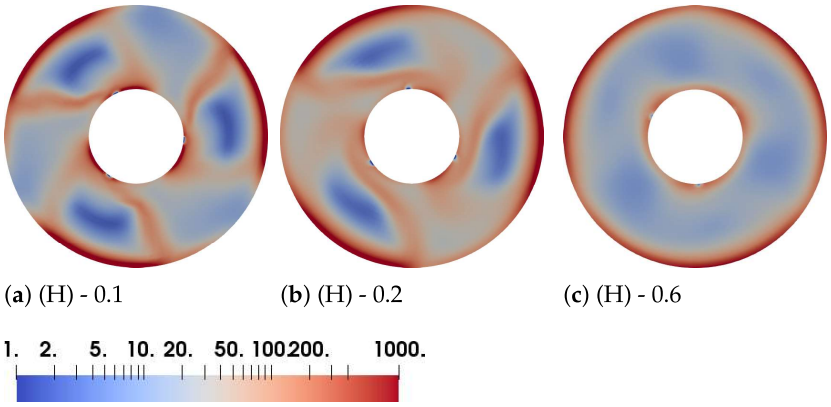

(**a**) (H) - 0.1 (**b**) (H) - 0.2 (**c**) (H) - 0.6

Figure 10. ε field for the (H) orientation at the three different positions along the prototype axis: 0.1 (**a**), 0.2 (**b**), and 0.6 (**c**).

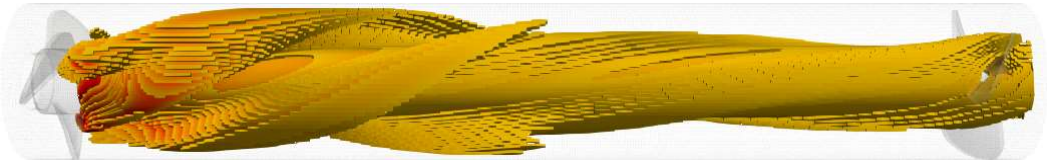

(**a**) (L) - 0.1

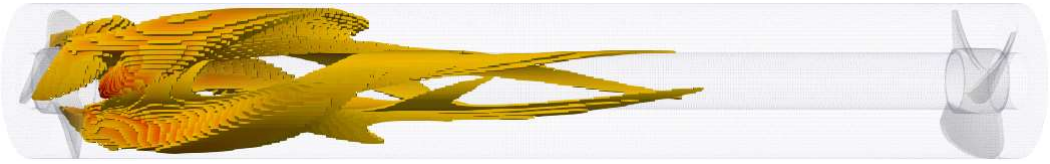

(**b**) (H) - 0.1

Figure 11. *Cont.*

(**c**) (L) - 0.2

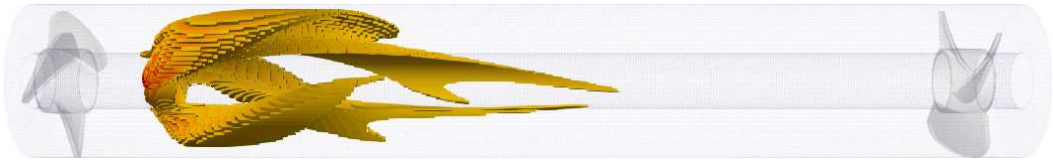

(**d**) (H) - 0.2

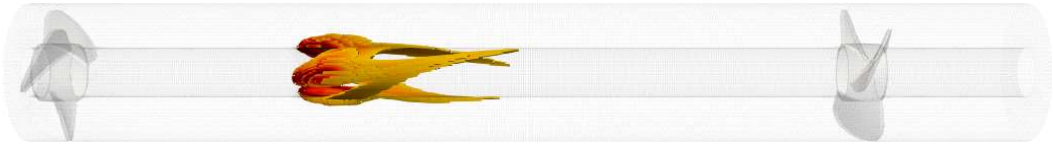

(**e**) (L) - 0.6

(**f**) (H) - 0.6

Figure 11. Spatial distribution of m_0 for the six simulations. Only volumes with $m_0 > 10^{18}$ particle no./m^3 are shown.

5. Discussion

The CFD-PBM framework developed in this study provides mechanistic insights into $Mg(OH)_2$ precipitation under varying feed concentrations and nozzle configurations. These findings are particularly relevant for the design and optimization of semi-continuous and continuous crystallization/precipitation processes in industrial applications such as wastewater treatment and magnesium recovery. From an industrial perspective, the results highlight the strong dependence of particle formation on mixing intensity and feed positioning. This suggests that engineering modifications, such as optimizing nozzle orientation, implementing multi-inlet configurations, or using recirculation loops, can effectively tailor the local supersaturation profile to favor desirable nucleation, growth, and aggregation pathways. For example, the use of angled or tangential feeds could help in homogenizing mixing zones while mitigating undesired aggregation. However, some limitations must be acknowledged. The current model assumes the PBM is one-way coupled to the flow field, neglecting the potential feedback of high solid loading on hydrodynamics. While this assumption is acceptable for the dilute conditions considered here, it may not hold for larger-scale reactors operating at a much higher throughput and some scale-up factors should be included. Additionally, the computational cost of the CFD-PBM simulations is not excessive, making this framework suitable for further investigations. Each CFD-PBM simulation required approximately 3 to 5 days of wall-

clock time using 16 CPU cores and 64 GB of RAM. This makes the framework tractable for mechanistic investigations and design studies, but potentially too slow for large-scale parameter identification or optimization tasks. Therefore, ongoing work is focused on developing machine learning surrogates to accelerate the design phase, as demonstrated in one of our previous publications [23]. Despite these limitations, the model provides a valuable mechanistic baseline that can be generalized to other precipitation systems, such as $CaCO_3$ and $BaSO_4$.

6. Conclusions

This study presents a CFD-PBM one-way coupled framework tailored toward detailing and optimizing the performance of a novel prototype for the recovery of Mg^{2+} from brines and bitterns. Beyond characterizing the prototype's complex hydrodynamics, we propose a series of modeling strategies and insights that can improve both fundamental understanding and smart reactor design. A key methodological contribution lies in the use of high-fidelity LES simulations to calibrate an RANS model capable of replicating the essential turbulence features at a significantly lower computational cost. This LES-calibrated RANS approach provides a practical yet accurate alternative to screening design variations in complex geometries when experimental validation is lacking. On the process side, our simulations reveal the non-intuitive effects of increased reactant concentrations: while higher molar flow rates nominally boost supersaturation, they can simultaneously hinder mixing, leading to negligible gains in precipitation rate. This highlights the importance of accounting for local micromixing dynamics rather than relying solely on bulk process variables. Furthermore, by varying the orientation and position of the nozzle, we can identify the crucial role of local turbulence dissipation rates in governing nucleation, growth, and aggregation processes. This leads to actionable guidance for reactor optimization: namely, that nozzle placement should be informed by the local turbulent energy dissipation field to maximize precipitation efficiency. This work demonstrates the value of combining advanced CFD modelling with PBM to support the smart manufacturing of crystallization and recovery processes in multiphase, turbulent systems.

7. Patents

The patent can be found through following this link: https://patents.google.com/patent/WO2022238913A1/en (accessed on 2 February 2024) and referring to Bevacqua et al. [26].

Supplementary Materials: The following supporting information can be downloaded at: https://www.mdpi.com/article/10.3390/pr13061721/s1, Figure S1: Monitoring lines selected downstream of the impellers for grid convergence analysis; Figure S2: Mesh visualization along the two monitoring lines for the three grid resolutions.

Author Contributions: Conceptualization, A.R.; methodology, A.R.; software, A.R.; validation, A.R.; formal analysis, A.R. and D.F.; investigation, A.R.; resources, F.V., A.C. and D.M.; data curation, A.R.; writing—original draft preparation, A.R.; writing—review and editing, A.R., F.V., A.C. and D.M.; visualization, A.R. and D.F.; supervision, A.R. and D.M.; project administration, A.C. and D.M.; funding acquisition, A.C. and D.M. All authors have read and agreed to the published version of the manuscript.

Funding: This project has received funding from the European Union's Horizon 2020 research and innovation programme under Grant Agreement No. 869467 (SEArcularMINE). This output reflects only the author's view. The European Health and Digital Executive Agency (HaDEA) and the European Commission cannot be held responsible for any use that may be made of the information contained therein.

Data Availability Statement: Data are available upon request.

Acknowledgments: A heartfelt thank you goes to Ing. Lorena Pasero for the fruitful discussions and feedback on the Design of Simulations. This project has received funding from the European Union's Horizon 2020 research and innovation programme under Grant Agreement No. 869467 (SEArcularMINE). This output reflects only the author's view. The European Health and Digital Executive Agency (HaDEA) and the European Commission cannot be held responsible for any use that may be made of the information contained therein. Computational resources were provided by HPC@POLITO, a project of Academic Computing within the Department of Control and Computer Engineering at the Politecnico di Torino (http://www.hpc.polito.it)).

Conflicts of Interest: Author Fabrizio Vicari was employed by the company ResourSEAs srl. The remaining authors declare that the research was conducted in the absence of any commercial or financial relationships that could be construed as a potential conflict of interest.

Abbreviations

The following abbreviations are used in this manuscript:

CFD	Computational Fluid Dynamics
PBM	Population Balance Model

References

1. Tai, C.M.; Li, R.K. Studies on the impact fracture behaviour of flame retardant polymeric material. *Mater. Des.* **2001**, *22*, 15–19. [CrossRef]
2. Béarat, H.; McKelvy, M.J.; Chizmeshya, A.V.; Sharma, R.; Carpenter, R.W. Magnesium hydroxide dehydroxylation/carbonation reaction processes: Implications for carbon dioxide mineral sequestration. *J. Am. Ceram. Soc.* **2002**, *85*, 742–748. [CrossRef]
3. Chen, X.; Yu, J.; Guo, S. Structure and properties of polypropylene composites filled with magnesium hydroxide. *J. Appl. Polym. Sci.* **2006**, *102*, 4943–4951. [CrossRef]
4. Zhang, S.; Cheng, F.; Tao, Z.; Gao, F.; Chen, J. Removal of nickel ions from wastewater by $Mg(OH)_2$/MgO nanostructures embedded in Al_2O_3 membranes. *J. Alloys Compd.* **2006**, *426*, 281–285. [CrossRef]
5. Gui, H.; Zhang, X.; Dong, W.; Wang, Q.; Gao, J.; Song, Z.; Lai, J.; Liu, Y.; Huang, F.; Qiao, J. Flame retardant synergism of rubber and $Mg(OH)_2$ in EVA composites. *Polymer* **2007**, *48*, 2537–2541. [CrossRef]
6. Kakaraniya, S.; Kari, C.; Verma, R.; Mehra, A. Gas absorption in slurries of fine particles: SO_2-$Mg(OH)_2$-$MgSO_3$ system. *Ind. Eng. Chem. Res.* **2007**, *46*, 1904–1913. [CrossRef]
7. Cao, H.; Zheng, H.; Yin, J.; Lu, Y.; Wu, S.; Wu, X.; Li, B. $Mg(OH)_2$ complex nanostructures with superhydrophobicity and flame retardant effects. *J. Phys. Chem. C* **2010**, *114*, 17362–17368. [CrossRef]
8. Sierra-Fernandez, A.; Gomez-Villalba, L.S.; Milosevic, O.; Fort, R.; Rabanal, M.E. Synthesis and morpho-structural characterization of nanostructured magnesium hydroxide obtained by a hydrothermal method. *Ceram. Int.* **2014**, *40*, 12285–12292. [CrossRef]
9. Song, X.; Tong, K.; Sun, S.; Sun, Z.; Yu, J. Preparation and crystallization kinetics of micron-sized $Mg(OH)_2$ in a mixed suspension mixed product removal crystallizer. *Front. Chem. Sci. Eng* **2013**, *7*, 130–138. [CrossRef]
10. Mullin, J.W. *Crystallization*; Elsevier: Amsterdam, The Netherlands, 2001.
11. Mersmann, A. *Crystallization Technology Handbook*; Marcel Dekker: New York, NY, USA, 2001; p. 832.
12. Baldyga, J.; Podgorska, W.; Pohorecki, R. Mixing-precipitation model with application to double feed semibatch precipitation. *Chem. Eng. Sci.* **1995**, *50*, 1281–1300. [CrossRef]
13. Marchisio, D.L.; Barresi, A.A.; Fox, R.O. Simulation of Turbulent Precipitation in a Semi-batch Taylor-Couette Reactor Using CFD. *AIChE J.* **2001**, *47*, 664–676. [CrossRef]
14. Marchisio, D.L.; Barresi, A.A.; Garbero, M. Nucleation, growth, and agglomeration in barium sulfate turbulent precipitation. *AIChE J.* **2002**, *48*, 2039–2050. [CrossRef]
15. Orlewski, P.M.; Mazzotti, M. Modeling of Mixing-Precipitation Processes: Agglomeration. *Chem. Eng. Technol.* **2020**, *43*, 1029–1039. [CrossRef] [PubMed]
16. Danckwerts, P. The effect of incomplete mixing on homogeneous reactions. *Chem. Eng. Sci.* **1958**, *8*, 93–102. [CrossRef]
17. Becker, G.W.; Larson, M.A. Mixing Effects in Continuous Crystallization. In *Crystallization from Solutions and Melts*; Palermo, J.A., Larson, M.A., Eds.; Springer: Boston, MA, USA, 1969; pp. 14–23. [CrossRef]
18. Battaglia, G.; Romano, S.; Raponi, A.; Volpe, F.; Bellanca, L.; Ciofalo, M.; Marchisio, D.; Cipollina, A.; Micale, G.; Tamburini, A. Mixing phenomena in circular and rectangular cross-sectional T-mixers: Experimental and numerical assessment. *Chem. Eng. Res. Des.* **2024**, *201*, 228–241. [CrossRef]

19. Schikarski, T.; Trzenschiok, H.; Peukert, W.; Avila, M. Inflow boundary conditions determine T-mixer efficiency. *React. Chem. Eng.* **2019**, *4*, 559–568. [CrossRef]
20. Schikarski, T.; Avila, M.; Trzenschiok, H.; Güldenpfennig, A.; Peukert, W. Quantitative modeling of precipitation processes. *Chem. Eng. J.* **2022**, *444*, 136195. [CrossRef]
21. Shiea, M.; Querio, A.; Buffo, A.; Boccardo, G.; Marchisio, D. CFD-PBE modelling of continuous Ni-Mn-Co hydroxide co-precipitation for Li-ion batteries. *Chem. Eng. Res. Des.* **2022**, *177*, 461–472. [CrossRef]
22. Raponi, A.; Romano, S.; Battaglia, G.; Buffo, A.; Vanni, M.; Cipollina, A.; Marchisio, D. Computational Modeling of Magnesium Hydroxide Precipitation and Kinetics Parameters Identification. *Cryst. Growth Des.* **2023**, *23*, 4748–4759. [CrossRef]
23. Raponi, A.; Marchisio, D. Deep learning for kinetics parameters identification: A novel approach for multi-variate optimization. *Chem. Eng. J.* **2024**, *489*, 151149. [CrossRef]
24. Raponi, A.; Achermann, R.; Romano, S.; Trespi, S.; Mazzotti, M.; Cipollina, A.; Buffo, A.; Vanni, M.; Marchisio, D. Population balance modelling of magnesium hydroxide precipitation: Full validation on different reactor configurations. *Chem. Eng. J.* **2023**, *477*, 146540. [CrossRef]
25. Battaglia, G.; Ventimiglia, L.; Vicari, F.; Tamburini, A.; Cipollina, A.; Micale, G. Characterization of $Mg(OH)_2$ powders produced from real saltworks bitterns at a pilot scale. *Powder Technol.* **2024**, *443*, 119918. [CrossRef]
26. Bevacqua, M.; Vassallo, F.; Cipollina, A.; Micale, G.; Tamburini, A.; Papapetrou, M.; Vicari, F. Reactor and Process for the Precipitation of a Solid Product, (ResourSEAs Srl), IT202100012473A. 2021. Available online: https://patents.google.com/patent/WO2022238913A1/en (accessed on 2 February 2024).
27. Maniscalco, F.; Buffo, A.; Marchisio, D.; Vanni, M. Numerical simulation of bubble columns: LES turbulence model and interphase forces blending approach. *Chem. Eng. Res. Des.* **2021**, *173*, 1–14. [CrossRef]
28. Pope, S. Ten Questions Concerning the Large-Eddy Simulation of Turbulent Flows. *New J. Phys.* **2004**, *6*, 35. [CrossRef]
29. David, R.; Marchal, P.; Klein, J.P.; Villermaux, J. Crystallization and precipitation engineering-III. A discrete formulation of the agglomeration rate of crystals in a crystallization process. *Chem. Eng. Sci.* **1991**, *46*, 205–213. [CrossRef]
30. Marchisio, D.L.; Pikturna, J.T.; Fox, R.O.; Vigil, R.D.; Barresi, A.A. Quadrature Method of Moments for Population-Balance Equations. *AlChE J.* **2003**, *49*, 1266–1276. [CrossRef]
31. Romano, S.; Trespi, S.; Achermann, R.; Battaglia, G.; Raponi, A.; Marchisio, D.; Mazzotti, M.; Micale, G.; Cipollina, A. The Role of Operating Conditions in the Precipitation of Magnesium Hydroxide Hexagonal Platelets Using NaOH Solutions. *Cryst. Growth Des.* **2023**, *23*, 6491–6505. [CrossRef]